

3D Computed Tomography Quantifies the Dependence of Bulk Porosity, Surface Roughness, and Re-Entrant Features on Build Angle in Additively Manufactured IN625 Lattice Struts

Tobias Fritsch,* Lena Farahbod-Sternahl, Itziar Serrano-Muñoz, Fabien Léonard, Christoph Haberland, and Giovanni Bruno

Layer-by-layer additive manufacturing (AM) by means of laser-powder bed fusion (L-PBF) offers many prospects regarding the design of lattice structures used, for example, in gas turbines. However, defects such as bulk porosity, surface roughness, and re-entrant features are exacerbated in nonvertical structures, such as tilted struts. The characterization and quantification of these kinds of defects are essential for the correct estimation of fracture and fatigue properties. Herein, cylindrical struts fabricated by L-PBF are investigated by means of X-ray computed tomography (XCT), with the aim of casting light on the dependence of the three kinds of defects (bulk porosity, surface roughness, and re-entrant features) on the build angle. Innovative analysis methods are proposed to correlate shape and position of pores, to determine the angular-resolved surface roughness, and to quantify the amount of re-entrant surface features, q . A meshing of the XCT surface enables the correlation of q with the classical surface roughness P_a . This analysis leads to the conclusion that there is a linear correlation between q and P_a . However, it is conjectured that there must be a threshold of surface roughness, below which no re-entrant features can be build.

such as lattice structures.^[4] These structures are suitable to be deployed in gas turbines, allowing reduction of weight as well as improvement of fuel premixing and heat transfer. All these aspects contribute to decrease emissions and improve total efficiency. These applications demand a detailed knowledge about the structural integrity of the lattice structures. Such integrity is strongly affected by bulk porosity, surface roughness, and re-entrant surface features, typical of L-PBF parts.

Lattice structures consist of small struts. Depending on the lattice design, each strut is processed with a certain tilt angle with respect to the build plate. Since post processing (e.g., sand blasting or polishing) is expensive and ineffective for these complex structures, the quality of as-built surfaces is of significant interest for the fatigue behavior of the lattice structure and for the gas flow through it.


The surface roughness of L-PBF parts has recently been discussed in several works.^[5–11] The arithmetic mean roughness value R_a is the most common parameter to describe the surface roughness.^[12] R_a is classically determined by tactile and optical measurement techniques. However, such techniques have

1. Introduction

Additive manufacturing (AM) by means of laser-powder bed fusion (L-PBF) allows an unprecedented freedom of design. This enables the production of parts with large complexity,^[1–3]

T. Fritsch, I. Serrano-Muñoz, F. Léonard, G. Bruno
Micro NDT
Bundesanstalt für Materialforschung und -prüfung (BAM)
Unter den Eichen 87, Berlin 12205, Germany
E-mail: tobias.fritsch@bam.de

L. Farahbod-Sternahl
Siemens Energy
Gas and Power
Huttenstraße 12, Berlin 10553, Germany

 The ORCID identification number(s) for the author(s) of this article can be found under <https://doi.org/10.1002/adem.202100689>.

© 2021 The Authors. Advanced Engineering Materials published by Wiley-VCH GmbH. This is an open access article under the terms of the Creative Commons Attribution License, which permits use, distribution and reproduction in any medium, provided the original work is properly cited.

DOI: 10.1002/adem.202100689

C. Haberland
Siemens Energy
Gas and Power
Mellinghofer Straße 55, Berlin 45473, Germany

F. Léonard
The University of Manchester at Harwell
Harwell Science and Innovation Campus
Didcot, Oxfordshire OX11 0DE, UK

G. Bruno
Institute of Physics and Astronomy
University of Potsdam
Karl-Liebknecht-Str.24-25, Potsdam 14476, Germany

shown limitations for the analysis of re-entrant features,^[6] which are specific to L-PBF parts, especially when overhanging and tilted structures are manufactured. The quantitative determination of such features has sparked a debate in the scientific community, so that the classic definition of surface roughness and its characteristics has been put under scrutiny or even declared invalid.^[12] Disregarding re-entrant features is dangerous as they are known to shorten the fatigue life of L-PBF parts.^[13] This work targets to fill this gap and aims to define an applicable and complementary parameter for re-entrant feature quantification.

It has been proven that X-ray computed tomography (XCT) measurements are in good agreement with conventional tactile surface measurements, for example, coordinate measuring machine (CMM) for flat surfaces. This agreement indicates the applicability of XCT for classic line-profile roughness analysis.^[14,15] XCT, thanks to its fully 3D capabilities, additionally enables the evaluation of inner surfaces,^[7,8] and re-entrant surface features.^[16,17] A method for the identification of re-entrant features by considering the direction of the surface normal has been discussed by Pagani et al.,^[16] who presented a mathematical definition of a re-entrant feature.

The surface quality is known to be influenced by the build angle,^[18,19] i.e., the angle between the part surface and the build plate. In the case of tilted structures, surfaces without supporting solid material during manufacturing are processed by the application of the so-called (tailored) down-skin (DS) scanning parameters, while surfaces without upper contact to the solid material during production are processed using the so-called up-skin (US) scanning parameters. DS surfaces have shown a higher mean roughness than US ones due to a larger number of attached isolated powder particles.

Based on these publications, we present a) a method for the quantification of re-entrant features for AM-surfaces, b) the application of the method for several lattice struts, and c) the correlation between the amount of re-entrant surface feature and

classical roughness values. Different build angles were used to obtain a systematic variation of the surface quality.

2. Experimental Section

The Ni-based alloy Inconel 625^[20] was used for L-PBF production of seven struts with different build angles α from 30° to 90° in steps of 10° (see **Figure 1a**), all other production parameters being the same. α was defined as the angle between the build baseplate and the nominal strut (cylinder) axis. Therefore, $\alpha = 90^\circ$ describes the strut built parallel to the build direction (BD). Each strut had nominal diameter of 1 mm and length of 6 mm. To avoid the effect of strut ends, a length of interest of 5 mm was analyzed. A circle segment, added to the CAD-file close to one end of the strut and used as a marker as shown in **Figure 1b**, was built together with the struts; a gap in the circle indicated the US direction. The struts were manufactured at Siemens Energy, Gas and Power, Berlin, Germany, within the same build job on an EOS M290 machine. No support structures and no contour scanning were used. A layer thickness of 20 μm along with Siemens-proprietary set of process parameter optimized for Inconel 625 were applied. These struts were always built tilted toward the re-coater movement axis.^[21]

XCT scans on the struts were conducted on a laboratory CT scanner (GE v|tome|x 300 L) using a transmission target (for the sake of high resolution). 125 kV and 65 μA were applied to the X-ray tube. The reconstruction was performed using a Feldkamp algorithm.^[22] The known and calibrated distance between a pair of ruby spheres allowed the calibration of the voxel size (determined to be 2.1 μm). Once the voxel size was calibrated, the rotation stage was held at a constant position for all XCT scans. The resolution in a single projection was determined to be 4 μm by using a JIMA RC-02 resolution chart.^[23] Three CT-scans were needed for each strut to capture the full strut length of 6 mm. All three single volumes were concatenated after reconstruction.

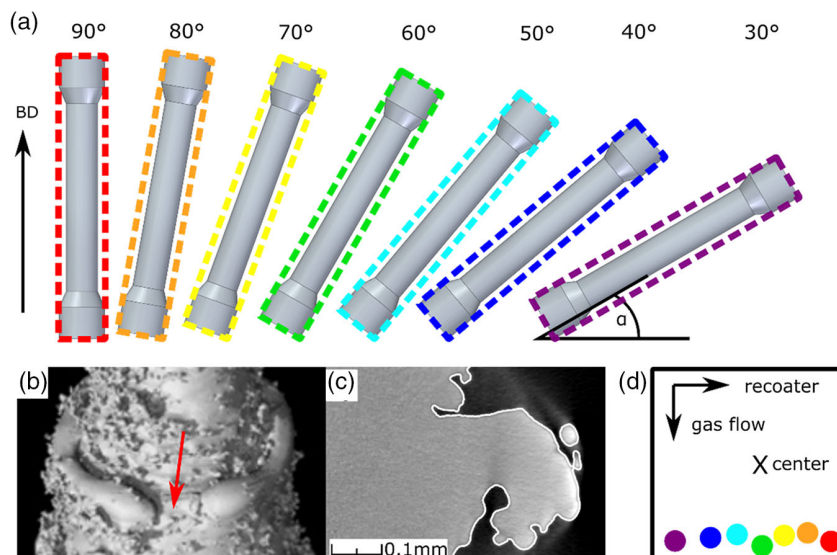


Figure 1. a) Sketch of the investigated struts with build angle α between 30° and 90° (BD = build direction), b) the gap in the reference marker circle (see red arrows) in 3D XCT reconstruction; c) a tomogram (i.e., tomographic slice, here perpendicular to the strut long axis) used to demonstrate the surface determination. d) Sketch of the seven struts positions on the build plate. The recoater and the gas flow axes are indicated.

The porosity analysis of the reconstructed struts was performed with the VGDefX- algorithm implemented in VG Studio Max 3.2. The smallest analyzed pore had a volume of 64 voxels to avoid false positive pore classification. The size of each pore was evaluated using the circumsphere diameter (i.e., the maximum diameter of the pore), the position within the strut together with the smallest distance to the strut surface in Euclidean space were recorded, and the shape was quantified in terms of the anisotropy, defined as

$$A = 1 - \frac{\lambda_3}{\lambda_1} \quad (1)$$

with λ_1 and λ_3 being the largest and the smallest eigenvalue of the covariance matrix, respectively, estimated by principal component analysis (PCA).^[24,25]

The advanced surface determination tool implemented in VG Studio Max 3.2 was used, as shown in Figure 1c. The surface was exported as both, a point cloud (ASCII format) and a meshed surface (triangular mesh in stl-format). The point cloud was used to analyze the roughness, and the meshed surface was used to analyze the re-entrant features (see below).

As a first step for the analysis of the strut roughness, the Cartesian strut surface (x, y, z) was converted into cylindrical coordinates $(\rho = \sqrt{x^2 + y^2}, \theta = \text{atan2}(y, x), z)$ for each point (x, y, z) of the surface (see Figure 2). Then, the primary line profiles of the surface along the strut length $\rho^\theta(z)$ were extracted for each azimuth angle θ (with a step width of 1° , i.e., 360 line profiles per strut). These line profiles $\rho^\theta(z)$ were analyzed by calculating the arithmetic mean primary profile $P_a(\theta)$

$$P_a(\theta) = \frac{1}{N} \sum_{i=1}^N |\rho_i^\theta(z) - \rho_{\text{mean}}^\theta| \quad (2)$$

with

$$\rho_{\text{mean}}^\theta = \frac{1}{N} \sum_{i=1}^N \rho_i^\theta(z) \quad (3)$$

where N is the number of pixels along z .

The struts were aligned using the reference marker (i.e., the gap in the circle segment) shown in Figure 1b, in such a way that

the DS lied along $\theta = 0^\circ$ and the US along $\theta = 180^\circ$. The reference marker allowed an alignment with a precision of $\pm 5^\circ$ in θ .

The meshed surface was analyzed as follows: A cylinder was fitted to each strut by the iterative closest point (ICP) algorithm. This is equal to the minimization of the squared difference between the actual surface (identified by XCT) and the cylinder surface for each point of the actual surface. The cylinder axis was then used as the center of the strut. We converted the meshed surface from Cartesian to cylindrical coordinates according to the transformation $(\rho = \sqrt{x^2 + y^2}, \theta = \text{atan2}(y, x), z)$ for each vertex of the meshed surface. Successively, we determined the center of mass (CM) and the direction of the normal vector for each triangle. The CM was needed to assign each triangle unambiguously to a certain line profile. All CMs lying within $\Delta\theta = 1^\circ$ were assigned to a certain line profile together with the areas of the corresponding triangles. If the ρ - (radial coordinate, not to be confused with the roughness) component of the normal-vector was negative, the triangle was indicated as a re-entrant feature, see Figure 2c. The area of these triangles was summed up along a line profile resulting in $A_{\rho < 0}^\theta$. Analogously, the area of all triangles along the same line profile was summed up resulting in A^θ . The ratio of the sum of the area of triangles with negative radial component ($A_{\rho < 0}^\theta$) and the sum of the area of all triangles (A^θ) assigned to each line profile was used in the quantification of the re-entrant features. The re-entrant feature ratio q was calculated as

$$q = \frac{A_{\rho < 0}^\theta}{A^\theta} \quad (4)$$

A similar definition of q has been introduced by Pagni et al.^[16] using 1D line profiles; here, we use the concept of meshed surface on the line profiles to generalize the definition.

3. Results

3.1. Roughness

The results of the primary profile (P_a) analysis according to Equation (2) are shown in Figure 3a. Most of the P_a values are found to be around 15–20 μm . Interestingly, for the DS region, significant deviations are observed over an azimuthal range of about $\theta \approx 90^\circ$ ($-45^\circ < \theta < 45^\circ$). This high roughness

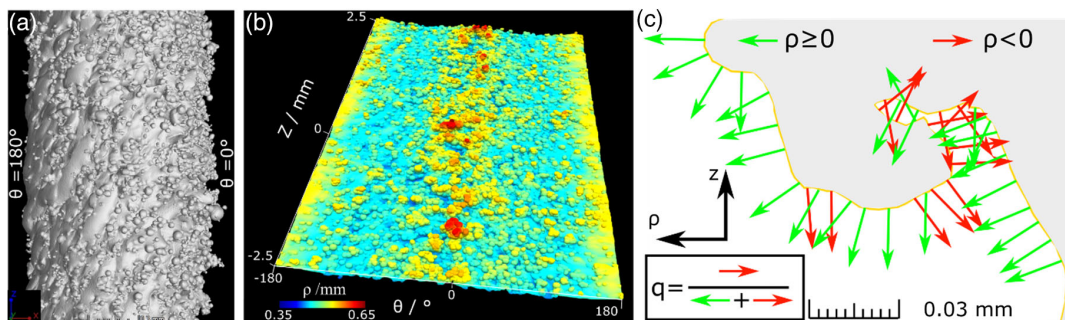


Figure 2. a) Side view of the rendered surface of the strut with $\alpha = 30^\circ$, aligned upright. The DS (right, $\theta = 0^\circ$) and the US (left, $\theta = 180^\circ$); b) the whole (unrolled) rendered surface presented in polar coordinates (ρ, θ, z) , and c) a sketch of the estimation of the re-entrant feature ratio q . The surface profile is taken from a reconstructed XCT slice.

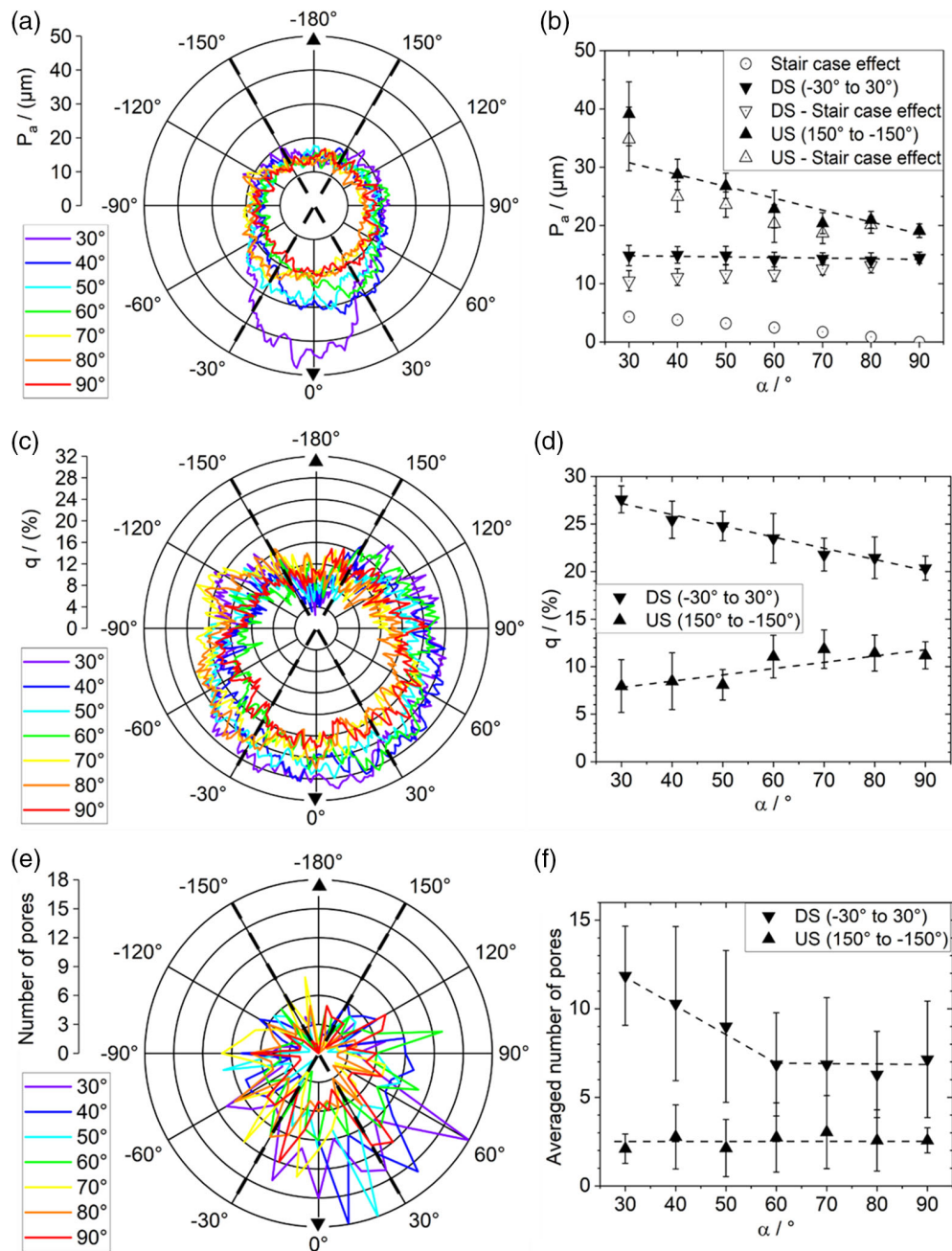


Figure 3. a) $P_a(\theta)$ as calculated according to Equation (2) as a function of α . The dotted lines indicate the sectors used for the analysis shown in (b). b) Dependence on the build angle α of the roughness parameter P_a for the US and the DS: the average of P_a in the DS region (θ between -30° and $+30^\circ$), and in the US (θ between -150° and $+150^\circ$) are displayed. c) $q(\theta)$ calculated according to Equation (4) as a function of α . The dotted lines indicate the sectors used for the analysis shown in (d). d) Dependence of the re-entrant feature parameter q for the US and the DS on the build angle α : the averages of q -value in the DS region (θ between -30° and $+30^\circ$), and in the US (θ between -150° and $+150^\circ$) are displayed. e) The number of pores was estimated by the VGdefX Algorithm (VG Studio 3.2 MAX) in dependence of θ . The dotted lines indicate the sectors used for the analysis shown in (f). f) Dependence of the number of pores for the US and the DS on the build angle α : the number of pores in the DS region (θ between -30° and $+30^\circ$), and US (θ between -150° and $+150^\circ$) are displayed.

indicates an increased number of attached powder particles over around a quarter of the strut surface.

For the US region no variation of P_a with the build angle was observed (see Figure 3a,b). However, after subtraction of the roughness induced by the so-called stair-case effect^[6] (round

markers in Figure 3b), a small increase of P_a as a function of α became visible, while the profile of P_a at the DS became slightly flatter. The correction method consists of the description of the stair-case effect with a step function. The height of a step corresponds to the layer thickness ($t_{\text{layer}} = 20 \mu\text{m}$) and the length of a

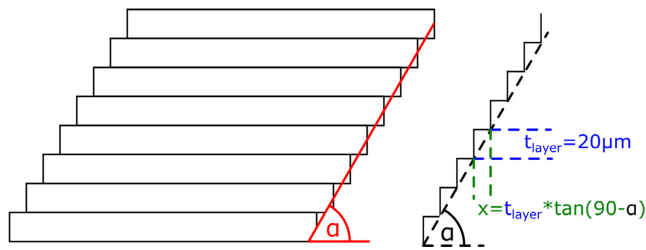


Figure 4. Illustration of the stair-case effect (left) and the representation of the respective surface profile (right). The surface profile is represented by a step function, which is defined by the layer thickness $t_{\text{layer}} = 20 \mu\text{m}$ and the build angle α . The step function was analyzed according to Equation (2) for P_a .

step $x = \tan(90 - \alpha) \cdot t_{\text{layer}}$ see **Figure 4**. This step function was then analyzed analogously to the other surface profiles according to Equation (2).

3.2. Re-Entrant Features

The results of the calculations of the re-entrant feature fraction q (according to Equation (4)) are shown in **Figure 3c**. At the US, q decreases with a decreasing α , whereas in the DS region it increases (see also **Figure 3d**). For all struts (i.e., independent of α), the values of q do not vary much as a function of θ for the whole DS region ($\theta = -90^\circ$ to $\theta = 90^\circ$). In fact, the most significant change in q is observed in the US region and it is limited to a small azimuthal range ($\Delta\theta \approx 60^\circ$).

3.3. Porosity

Figure 3e shows the angular distribution of the number of pores. The integrated number of pores within a strut segment of 10° in the hoop direction θ and 5 mm in height z was calculated for all seven struts. For the comparison of the seven build angles, the

Table 1. The volume of material investigated for porosity for each strut.

α [°]	30	40	50	60	70	80	90
Volume [mm ³]	4.13	4.34	4.19	4.07	4.07	4.01	3.94

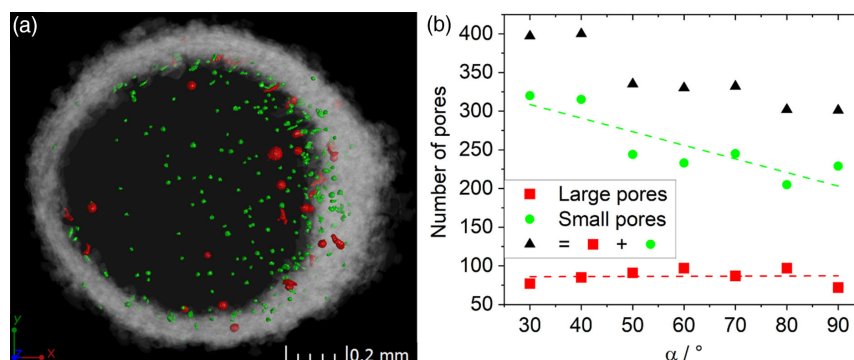


Figure 5. a) Projection of pores along the height of the strut with $\alpha = 30^\circ$. The solid material is presented with a transparency of 90% (black, in the center). The pores are color-coded according to two categories: small ($\leq 30 \mu\text{m}$, green) and large ($> 30 \mu\text{m}$, red). b) Absolute number of small and large pores in dependence of the build angle α . The dashed lines represent respective linear fits.

number of pores were averaged in the US region between $150^\circ < \theta < -150^\circ$ and in the DS region between $-30^\circ < \theta < 30^\circ$). These average values are presented with their standard deviations as error bars in **Figure 3f**. Even though the standard deviations are large due to weak statistics, two statements can be made: a) a larger number of pores is present in the DS region than in the US region, and b) while the average number of pores in the DS region decreases with α , it remains constant in the US region.

The material volume investigated is similar for all struts, see **Table 1**.

In **Figure 5a**, the pores and the surface of the strut with $\alpha = 30^\circ$ are presented as a projection along the length of the strut. The pores are color-coded according to their size (green for size $\leq 30 \mu\text{m}$ and red for size $> 30 \mu\text{m}$). The surface is represented as a cloud as it does not lie at the same position in each coordinate along the height (the projection direction). In this sense, the cloud gives a pictorial idea of the variation of the surface position along the height at each azimuth angle and shows that the minimum cross-section (a capital information for the determination of the strut strength) is far from the nominal one.

The values of the number of pores (above the XCT data resolution) for all struts are summarized in **Figure 5b**. Both, the total number of pores and the number of small and large pores are presented in dependence of α . The decrease in the total number of pores is in fact directly determined by the reduction in the number of small pores. The number of large pores remains constant with α . In combination with the spatial distribution of porosity (**Figure 3a**), we can conclude that a tilted build job ($\alpha \neq 90^\circ$) mainly promotes pores with sizes $< 30 \mu\text{m}$ in the DS region.

Figure 5 shows the degree of anisotropy (A) as a function of the distance to the sample surface of each segmented pore. Most of the pores accumulate within $90 \mu\text{m}$ from the surface (region I). This effect is known and explained by the excessive energy input and heat accumulation.^[26] Since a low anisotropy A means nearly spherical pores, we observe an absence of elongated pores at large distance to the sample surface (region II). This indicates a preferential appearance of elongated pores ($A \geq 0.8$) within less than $90 \mu\text{m}$ to the surface. Nearly every pore with a distance to the strut surface that is larger than $90 \mu\text{m}$ showed an anisotropy value lower than 0.8 (region III). These

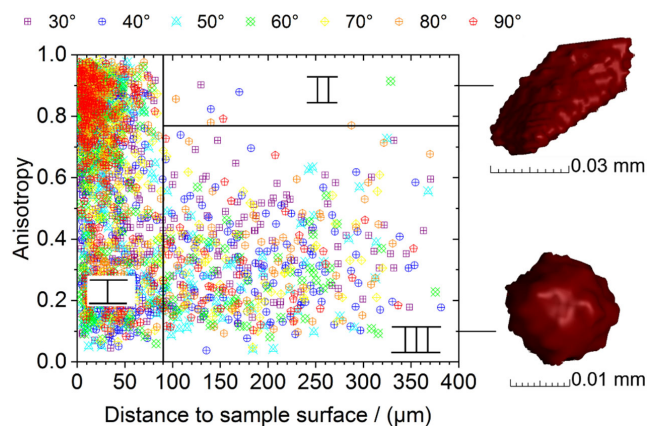


Figure 6. The anisotropy A plotted as a function of distance to the sample surface, i.e., the smallest distance (in 3D) between pore surface and sample surface. Each point corresponds to one pore in the 3D XCT reconstruction.

two facts imply that pores near the sample surface may suffer from an anisotropic heat flow, whereas central sample regions undergo isotropic heat flow, so that pores remain spherical. A systematic study on such effects is, however, needed to arbitrate on the matter.

A dependence of the pore shape and the pore position on the build angle is not visible in **Figure 6**. The tilt of the struts seems to influence neither of them, and we can conclude that the pore shape and position mostly depend on the printing parameters.

4. Discussion

For the strut with $\alpha = 90^\circ$, the mean roughness parameter P_a was expected to be the same in every direction (i.e., independent of θ in **Figure 3c**, $P_a(\theta) = \text{constant}$). However, a significant difference of P_a between $\theta = 180^\circ$ and $\theta = 0^\circ$ is observed. Indeed, the strut with $\alpha = 90^\circ$ was located in a corner of the build plate (see **Figure 1d**). Hence, the laser beam approximately penetrated with an angle of 15° into the powder bed. This tilted penetration of the laser beam into the powder bed causes a

distortion of the energy spatial distribution profile. A similar effect has been observed in Kleszczynski et al.^[11]

An effect of the position on the porosity distribution cannot be fully discarded, and this is why we would expect the same effect on the other struts as well. Indeed, if we look at **Figure 3f**, we observe no porosity difference among the struts tilted 60° – 90° . For these struts, the effect of the build angle and of the position on the base plate on the porosity should balance each other. In the tilt interval 30° – 50° , it seems that the strut tilt has more impact on the pore distribution than the strut position. It should also be emphasized that the statistics of porosity are low.

In general, both the polar diagrams of the roughness (**Figure 3c**) and of the amount of re-entrant features (**Figure 3e**) show better surface quality at the US than at the DS. The largest values of both P_a and q are found at the DS for the 30° strut. Both P_a and q polar diagrams are symmetric with respect to $\theta = 0^\circ$ for each strut (i.e., they have the same values, e.g., for $\theta = 90^\circ$ and $\theta = -90^\circ$). However, some characteristic differences lead to new information about the surface topography.

At the DS ($\theta = 0^\circ$), the ratio $q(\alpha = 30^\circ)/q(\alpha = 90^\circ)$ is only about 1.2 (**Figure 3d**), whereas the ratio $P_a(\alpha = 30^\circ)/P_a(\alpha = 90^\circ)$ is about 2 (see **Figure 3b**) after the correction by the stair-case effect. It is known that the amount of attached powder particles increases at the DS. We, therefore, conclude that the P_a parameter is more sensitive to attached powder particles than q . This particular sensitivity could depend on the fact that q is a ratio between the re-entrant feature and the total surfaces, and attached powder particles would increase both, while P_a solely depends on the height of the attached powder particles.

At the US ($\theta = 180^\circ$), on the contrary, we observe no dependence of P_a on α (see **Figure 3b,d**), i.e., $P_a(\alpha = 30^\circ)/P_a(\alpha = 90^\circ) \approx 1$, whereas q increases with α , and $q(\alpha = 30^\circ)/q(\alpha = 90^\circ) \approx 0.5$. This indicates an improvement of the US-surface for tilted structures, which cannot be deduced from the P_a data alone. We, therefore, conclude that neither P_a nor q alone is sufficient to fully represent the surface quality, and the two quantities yield complementary information. Even further, we show that P_a should not be discarded as a metric for the surface roughness, but only complemented by q .

Indeed, the two quantities do depend from one another. The correlation between P_a - and q -values averaged over each line scan

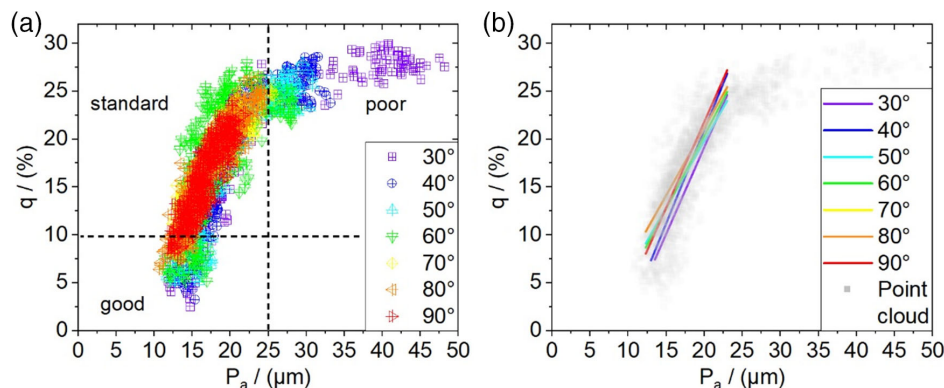


Figure 7. a) The correlation between the re-entrant feature ratio q and surface roughness P_a is shown. Each point corresponds to one analyzed line profile whereas the color depicts the build angle α . The dashed lines indicate different regions of the point clouds. b) The principal axes are presented for the “standard” region of the point clouds. The data points from (a) are shown transparent.

is shown in **Figure 7a**. These point clouds were analyzed by means of a PCA in the region $P_a < 25 \mu\text{m}$ and $q > 10\%$. The main axes of the PCA for all α are shown in **Figure 7b**. The plots prove that the higher the roughness, the higher the relative number of re-entrant features on the surface. However, we notice four important features: 1) A lower threshold of P_a between 10 and 15 μm seems to be present. While this aspect would need further investigation, it is reasonable to conclude that re-entrant features start building up only above a certain roughness. 2) The correlation between q and P_a is independent of the build angle. In the range $P_a < 25 \mu\text{m}$, the point clouds themselves have the same location in the graph (i.e., mean values of the point cloud) and direction of the main axes for all build angles. The build angles determine the quality of the surface: small build angles (e.g., 30°) lead to more points in the region of the q versus p plot at $P_a > 25 \mu\text{m}$, $q > 25\%$. Unfortunately, the statistics are not good enough in this region of the plot to carry out a robust PCA. This would be the part of future work. 3) The slope changes abruptly at P_a at 25 μm . This implies that at values of the primary profile in slight excess of the layer thickness, the strong correlation between roughness and amount of re-entrant feature disappears. In other words, for (large) roughness values, beyond the layer thickness, no further re-entrant features can be created. Even if this correlation between layer thickness and re-entrant features saturation threshold needs to be further investigated, it is reasonable to argue that as re-entrant features are generated by overhanging powder particles, the probability of forming a chain of hanging powder particles is very low. 4) An upper limit for q (around 30%) is observed; in the region of large P_a , even a drastic increase of the roughness, for example, by an increased number of attached powder particles, would not lead to more than one-third of the surface area being re-entrant. We cannot conclude whether this fact can be generalized to other metallic materials, and this would be the subject for further systematic investigations.

These results lead us to a significant classification: L-PBF surfaces could be distinguished into three levels of surface quality: 1) “good” surfaces with no re-entrant features and P_a below 10 μm (representing most likely horizontal structures); 2) “standard” surfaces with up to 25% re-entrant features and P_a between 10 and 25 μm (representing side walls and tilted surfaces up to $\alpha = 70^\circ$); and 3) “poor” surfaces, with a quarter to a third re-entrant features and P_a above 25 μm (representing overhanging structures or large tilt angles, $\alpha < 40^\circ$).

Actually, the fact that no data are available in the region with $P_a < 10 \mu\text{m}$ and $q < 5\%$ means that as-built AM surfaces can rarely be classified as “good”. On the other hand, even an unrealistic increase of P_a (of more than twice the size of the layer thickness) would not engender more re-entrant features.

The effect of the statistics of the point cloud in **Figure 7a** was negligible. A decrease of the number of line scans analyzed (i.e., the use of 72 ($\Delta\theta = 5^\circ$) instead of 360 ($\Delta\theta = 1^\circ$) line profiles for the analysis of each strut) lead just to a decreased spread of the data.

The aforementioned findings are particularly valuable in the case of lattice structures: Struts are manufactured in any case with a tilt with respect to the BD. The understanding of the correlation between surface quality in single strut and the respective build angle would enable the optimization of both the build job

and the whole design of the lattice structure also eliminating the need for impractical surface treatments.

5. Conclusion

The porosity, surface roughness, and re-entrant features were analyzed and quantified for the as-build condition of struts (meant to be implemented in lattice structures) build with seven different build angles.

The porosity was proven to depend on the build angle in terms of pore size in the down-skin region only. While at down-skin, the number of pores $< 30 \mu\text{m}$ decreased with increasing build angle, at the up-skin the number stayed constant. The combined analysis of all seven struts led to the conclusion that the elongated pores, with an anisotropy of 0.8 or higher, are abundant at a distance to the surface less than 90 μm , even though no contour scanning was applied during production.

In agreement with existing literature for tilted struts, we observed a surface roughness increase at the down-skin surface and no dependence on the build angle at the up-skin. The surface analysis was advanced with a new method for the quantification of re-entrant features based on surface triangulation. This relative amount of re-entrant features q showed an improvement at the US up-skin surface for tilted struts, as it would be expected for the L-PBF process. We observed that for L-PBF IN625 three regions can be distinguished in the roughness space: 1) a region of low roughness (corresponding to $\frac{1}{2}$ of the layer thickness), where no re-entrant features occur; 2) a region of linear correlation between roughness and amount of re-entrant features; and 3) a region (where the roughness exceeds the layer thickness) where no further re-entrant features can be created, irrespective of the increase of roughness.

The correlation of the conventional surface roughness parameter P_a and the new re-entrant feature parameter q enables the identification of three different surface quality levels (good, standard, and poor).

Indeed, P_a and q result complementary for the quantification of AM-surface quality, and, separately, each of them yields invaluable information.

Acknowledgements

F.L. acknowledges the funding from the EMPIR program co-financed by the Participating States and from the European Union's Horizon 2020 research and innovation program (15HLT09).

Open access funding enabled and organized by Projekt DEAL.

Conflict of Interest

The authors declare no conflict of interest.

Author Contributions

Conceptualization: All authors contributed to the content of the paper. Investigation: T.F., L.F.S., F.L., and C.H. were involved in the sample design, sample production, computed tomography measurements, and post-treatment of the acquired data. Visualization: T.F. and I.S.M. prepared and created the data visualization. Writing—original draft: T.F.

wrote the initial draft of this work. Writing—review and editing: All authors reviewed and commented on the work. Supervision: T.F., C.H., and G.B. supervised the work.

Data Availability Statement

Data is available on request from the authors.

Keywords

additive manufacturing, computed tomography, laser-powder bed fusion, re-entrant features, surface roughness

Received: June 2, 2021

Revised: September 9, 2021

Published online:

-
- [1] T. T. Wohlers, *3D Printing State Ind.* **2013**, 1, 2.
- [2] J. Gausemeier, N. Echterhoff, M. Wall, *Additive Manufacturing, RTejournal - Forum für Rapid Technologie*, Aachen, Germany, **2013**, p. 296.
- [3] I. Gibson, D. Rosen, B. Stucker, *Additive Manufacturing Technologies*, Springer, New York, **2015**.
- [4] H. Brodin, J. Saarimäki, in *13th International Conf. on Fracture*, International Congress on Fracture (ICF), Cassino, Italy, Beijing, China **2013**.
- [5] H. Shipley, D. McDonnell, M. Culleton, R. Coull, R. Lupoi, G. O'Donnell, D. Trimble, *Int. J. Machine Tools Manuf.* **2018**, 128, 1.
- [6] Z. Chen, X. Wu, D. Tomus, C. H. J. Davies, *Addit. Manuf.* **2018**, 21, 91.
- [7] A. Townsend, L. Pagani, P. Scott, L. Blunt, *Precision Eng.* **2016**, 48, 254.
- [8] A. Thompson, L. Körner, N. Senin, S. Lawes, I. Maskery, R. Leach, in *7th Conf. on Industrial Computed Tomography*, **2017**.
- [9] M. Suard, G. Martin, P. Lhuissier, R. Dendievel, F. Vignat, J. J. Blandin, F. Villeneuve, *Addit. Manuf.* **2015**, 8, 124.
- [10] T. Grimm, G. Wiora, G. Witt, *Surf. Topogr.: Metrol. Prop.* **2015**, 3, 014001.
- [11] S. Kleszczynski, A. Ladewig, K. Friedberger, J. Z. Jacobsmühlen, D. Merhof, G. Witt, in *26th Int. Solid Free Form Fabrication Symp.*, Austin, TX **2015**, pp. 360–370.
- [12] A. Townsend, N. Senin, L. Blunt, R. K. Leach, J. S. Taylor, *Precis. Eng.* **2016**, 46, 34.
- [13] J. Gockel, L. Sheridan, B. Koerper, B. Whip, *Int. J. Fatigue* **2019**, 124, 380.
- [14] H. Villarraga-Gómez, C. Lee, S. T. Smith, *Precis. Eng.* **2018**, 51, 291.
- [15] B. Gapinski, M. Wieczorowski, L. Marciniak-Podszadna, B. Dybala, G. Ziolkowski, *Procedia Eng.* **2014**, 69, 255.
- [16] L. Pagani, A. Townsend, W. Zeng, S. Lou, L. Blunt, X. Q. Jiang, P. J. Scott, *Measurement* **2019**, 141, 442.
- [17] F. Zanini, L. Pagani, E. Savio, S. Carmignato, *CIRP Annals* **2019**, 68, 515.
- [18] I. Koutiri, E. Pessard, P. Peyre, O. Amlou, T. De Terris, *J. Mater. Proc. Technol.* **2018**, 255, 536.
- [19] G. Pyka, A. Burakowski, G. Kerckhofs, M. Moesen, S. Van Bael, J. Schrooten, M. Wevers, *Adv. Eng. Mater.* **2012**, 14, 363.
- [20] T. Thiede, T. Mishurova, S. Evseev, I. Serrano-Munoz, C. Gollwitzer, G. Bruno, *Quantum Beam Sci.* **2019**, 3, 3.
- [21] L. Farahbod, T. Thiede, D. Rule, C. Haberland, S. Piegert, G. Witt, *DDMC*, Fraunhofer Verlag, Stuttgart, Berlin, Germany **2018**.
- [22] L. A. Feldkamp, L. C. Davis, J. W. Kress, *J. Opt. Soc. Am. A* **1984**, 1, 612.
- [23] V. Voland, M. Salamon, S. Reisinger, S. Schröpfer, N. Uhlmann, in *Novel Techniques for High-Resolution Computed Tomography of Optoelectronic Devices*, **2012**.
- [24] I. Jolliffe, *Principal Component Analysis*, Springer, Berlin **2011**.
- [25] W. Feller, *An Introduction to Probability Theory & Its Applications*, South Asia Books CRC press, Boca Raton, Florida, **1991**.
- [26] A. A. Martin, N. P. Calta, S. A. Khairallah, J. Wang, P. J. Depond, A. Y. Fong, V. Thampy, G. M. Guss, A. M. Kiss, K. H. Stone, C. J. Tassone, J. N. Weker, M. F. Toney, T. van Buuren, M. J. Matthews, *Nat. Commun.* **2019**, 10, 1987.